CHEMISTRY OF MATERIALS

pubs.acs.org/cm

Article

Induced Mineralization of Hydroxyapatite in *Escherichia coli* Biofilms and the Potential Role of Bacterial Alkaline Phosphatase

Laura Zorzetto,* Ernesto Scoppola, Emeline Raguin, Kerstin G. Blank, Peter Fratzl, and Cécile M. Bidan

Cite This: *Chem. Mater.* 2023, 35, 2762−2772

Read Online

ACCESS | Metrics & More | Article Recommendations | Supporting Information

ABSTRACT: Biofilms appear when bacteria colonize a surface and synthesize and assemble extracellular matrix components. In addition to the organic matrix, some biofilms precipitate mineral particles such as calcium phosphate. While calcified biofilms induce diseases like periodontitis in physiological environments, they also inspire the engineering of living composites. Understanding mineralization mechanisms in biofilms will thus provide key knowledge for either inhibiting or promoting mineralization in these research fields. In this work, we study the mineralization of *Escherichia coli* biofilms using the strain *E. coli* K-12 W3110, known to produce an amyloid-based fibrous matrix. We first identify the mineralization conditions of biofilms grown on nutritive agar substrates supplemented with calcium ions and β-glycerophosphate. We then localize the mineral phase at different scales using light and scanning electron microscopy in wet conditions as well as X-ray microtomography. Wide-angle X-ray scattering enables us to further identify the mineral as being hydroxyapatite. Considering the major role played by the enzyme alkaline phosphatase (ALP) in calcium phosphate precipitation in mammalian bone tissue, we further test if periplasmic ALP expressed from the *phoA* gene in *E. coli* is involved in biofilm mineralization. We show that *E. coli* biofilms grown on mineralizing medium supplemented with an ALP inhibitor undergo less and delayed mineralization and that purified ALP deposited on mineralizing medium is sufficient to induce mineralization. These results suggest that also bacterial ALP, expressed in *E. coli* biofilms, can promote mineralization. Overall, knowledge about hydroxyapatite mineralization in *E. coli* biofilms will benefit the development of strategies against diseases involving calcified biofilms as well as the engineering of biofilm-based living composites.

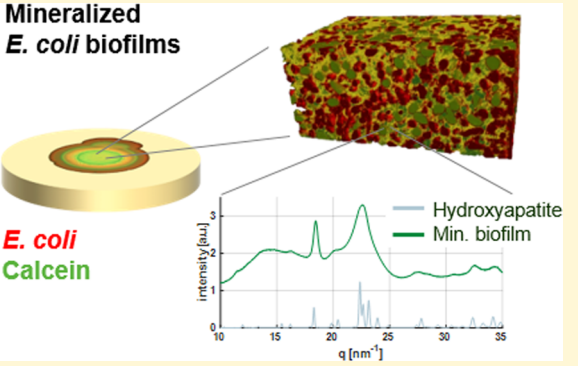

INTRODUCTION

Microbial biofilms form when bacteria colonize a surface and synthesize extracellular matrix components to survive challenging environments.[1] In addition to the organic matrix, some biofilms accumulate mineral particles.[2] Microbial mineralization results from adventitious precipitation of inorganic compounds led by their interactions with different metabolic processes and is defined as "biologically induced mineralization."[3,4] The most common minerals deposited by bacteria are calcium carbonates and calcium phosphates,[3] and they usually accumulate on the surface of the bacteria (epicellular mineralization), which then become embedded in the growing crystals.[3,5] Understanding the process of mineral deposition in bacterial biofilms is important for a number of reasons. On the one hand, pathological mineralization may lead to a wide range of diseases, including dental calculus[6] that can be associated with serious conditions like periodontitis.[7] Kidney stones are other examples of mineralized biofilms that form in physiological environments.[8] On the other hand, bacterial biofilms are living materials with potential technical applications. Here, mineralization may serve as one possible strategy to modify their mechanical and other physical properties.[9,10]

Pathological calculi have been described from the mineral and microbiological points of view; yet, how mineralization is triggered is still unclear.[11] Kidney stones have been historically linked to ion supersaturation in urine. While this remains considered as a risk factor,[12] recent research showed that mineral precursor supersaturation is actually not more frequent in patients developing kidney stone disease than in control groups.[8,13,14] This observation encouraged scientists to reconsider the role of bacteria in kidney stone formation, where bacteria may not only become trapped but could also play a significant role in stone growth.[8,15,16]

While the induction of calcium carbonate precipitation by *Bacillus subtilis* and *Escherichia coli* has been studied in the context of living and self-repairing materials,[17,18] the present study focuses on calcium phosphates, which are also

Received: September 28, 2022
Revised: March 22, 2023
Published: March 31, 2023

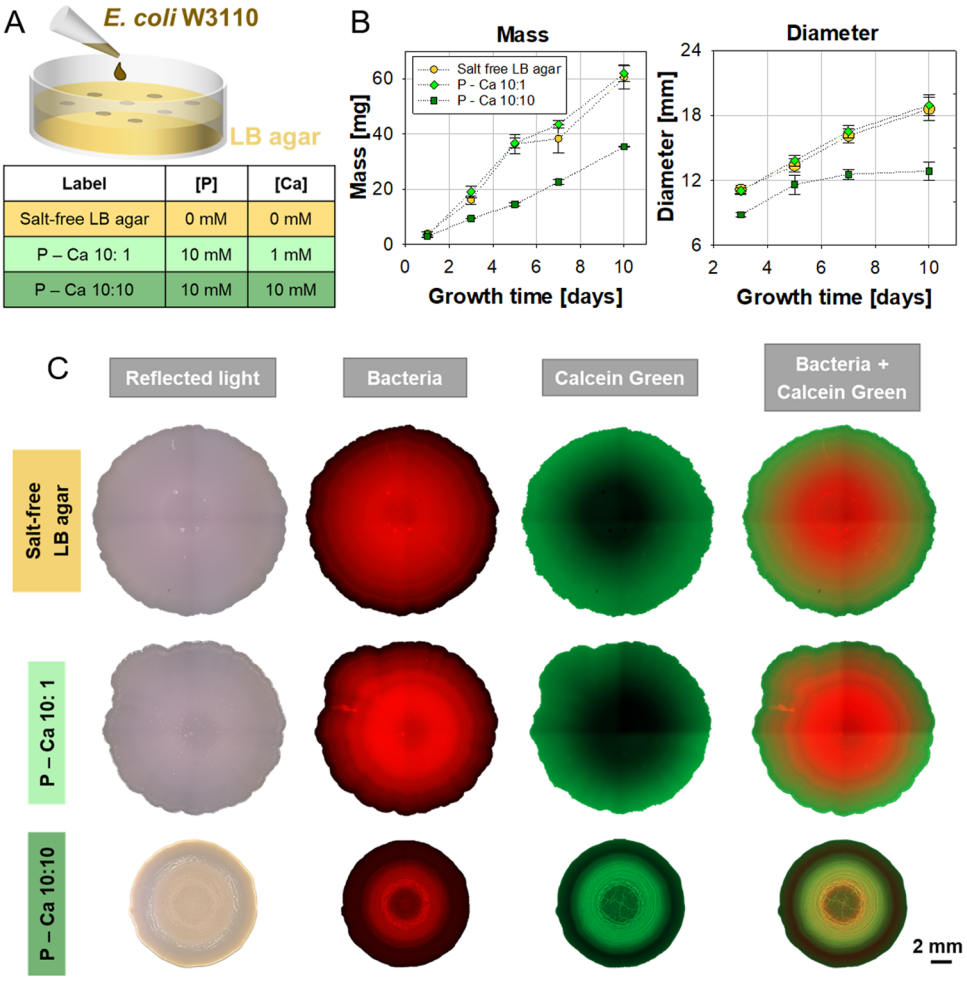

Figure 1. Detection of mineralization depending on different culturing conditions. (A) Overview of the composition of the nutritive substrates with the respective Ca^{2+} ions and β-glycerophosphate concentrations. (B) Diameter and wet mass of the biofilms, respectively, estimated from the stereomicroscopy images and by gravimetry. (C) Stereomicroscopy of biofilms after 10 days of growth in different conditions. Shown is the reflected light (first column), mCherry fluorescence to highlight the presence of bacteria (second column), Calcein fluorescence (third column), and overlaid mCherry and Calcein fluorescence (fourth column).

widespread and widely studied in the eukaryotic world.[19] In saliva, for example, mineral precursors for hydroxyapatite (HA), octacalcium phosphate, and whitlockite are present in supersaturated concentrations. These are the most frequent calcium phosphate crystal phases found in dental calculus.[20] However, the concentrations of calcium and phosphate ions are not high enough to cause spontaneous precipitation.[21] Recently, alkaline phosphatase (ALP) has been identified as an indicator of periodontitis,[22] which suggests that bacteria from the oral microbiome could exploit similar mechanisms as eukaryotic cells (e.g., bone cells) to induce mineral deposition in the mouth. In mammalian bone, indeed, calcium phosphates are deposited in the form of HA through a finely tuned process that results in a functional material with high levels of spatial organization, complex morphologies, and well-defined crystallo-chemical properties.[23] This process is defined as "biologically controlled mineralization," in contrast to the adventitious "biologically induced mineralization" happening in most prokaryotes.[3] Bone-specific ALP plays a key role in HA precipitation. It catalyzes the hydrolysis of polyphosphates and phosphate esters from organic sources (e.g., alkaloids, proteins) and makes them available for the interaction with cations (e.g., calcium).[11,24−26] Bacterial ALPs are either found intracellularly, in the periplasmic space of Gram-negative bacteria (e.g., *E. coli*),[27,28] or extracellularly, either as secreted enzymes or bound to the cell surface (e.g., *S. aureus*).[29,30] In *E. coli*, periplasmic ALP is encoded by the *phoA* gene.[27] PhoA was shown to induce HA formation in the presence of individual *E. coli* bacteria;[31] but, its role in biofilm formation remains to be investigated, as has recently been done for *S. aureus* biofilms.[24,32]

In this work, we used the *E. coli* K-12 strain W3110 that produces a matrix made of amyloid fibers (curli fibers) and expresses periplasmic PhoA (from now on referred to as ALP)[33] to grow biofilms on nutritive agar substrates supplemented with calcium chloride and β-glycerophosphate as an organic source of phosphates.[31] The presence and distribution of minerals in the biofilms were detected via Calcein fluorescence. At smaller length scales, the minerals were localized by X-ray microtomography and focused ion beam with scanning electron microscopy in cryo-conditions (cryo-FIB-SEM). Wide-angle X-ray scattering (WAXS) enabled us to identify the mineral phase as HA. The role of ALP in biofilm mineralization is supported by the lack of HA in biofilms grown on mineralizing medium supplemented with an ALP inhibitor. Furthermore, HA formation was also

https://doi.org/10.1021/acs.chemmater.2c02969
Chem. Mater. 2023, 35, 2762−2772

observed when depositing a droplet of purified bacterial ALP on the mineralizing medium.

RESULTS

***E. coli* Biofilms Mineralize in the Presence of Calcium and β-Glycerophosphate.** To determine the mineralization conditions of *E. coli* biofilms at the solid−air interface, we first used Luria Bertani (LB) agar substrates deprived of sodium chloride but supplemented with calcium ions and sodium β-glycerophosphate at different concentrations (Figure 1A). The β-glycerophosphate concentration was set to 10 mM. This value approaches the physiological concentration of phosphate in human saliva[20] and is identical to the phosphate concentration at which *E. coli* can mineralize in liquid medium.[31] Despite not being naturally present in mammalian saliva, β-glycerophosphate is traditionally used as a model for the organic source of phosphates in dental plaque calcification.[34,35] Two concentrations of calcium chloride were tested: a concentration of 1 mM corresponding to the typical ion concentration in human saliva[20,36] (experiment named P-Ca 10:1) and a concentration of 10 mM, which has previously been used to induce mineralization in liquid medium[31] (experiment named P-Ca 10:10). Finally, salt-free LB agar was used as a control condition (nonmineralizing medium). To localize mineral precipitation, Calcein Green (4 μM) was added to the nutritive medium as an indicator of extracellular calcium accumulation.[37] We seeded the different agar substrates with suspensions of *E. coli* W3110 that constitutively expresses the fluorescent protein mCherry in their cytoplasm and imaged the biofilms at different time points during 10 days of growth. Biofilms grew from the initial inoculation trace up to a diameter of about 18−19 mm within 10 days (Figure 1B). Biofilms grown on the medium with a lower Ca^{2+} concentration (P-Ca 10:1) did not show any relevant differences in mass and final size with respect to salt-free agar. Biofilms grown on the medium with a higher Ca^{2+} concentration (P-Ca 10:10) had a smaller final diameter and lower mass compared to the other two conditions.

After 10 days of growth (Figure 1C), mCherry fluorescence indicated that most of the bacteria were concentrated in the center of the biofilm. In contrast, in biofilms grown on the control medium or on the medium with a lower Ca^{2+} concentration (P-Ca 10:1), Calcein fluorescence indicated higher Ca^{2+} concentrations at the biofilm periphery. Considering that the Calcein green used here should not penetrate the bacterial cells, these opposite distribution patterns of bacteria and Ca^{2+} are consistent with the diffusion of Ca^{2+} from the medium into the biofilm, where regions highly populated with bacteria are expected to show less Calcein signal. The emergence of these characteristic distributions is also shown in Figure S1, which reports fluorescence images taken at different times of growth (from day 3 to day 10). In biofilms grown in the P-Ca 10:10 condition, an overall higher Calcein signal was expected due to the larger presence of calcium in the medium. However, the Calcein signal appeared much brighter in the biofilm center and partially colocalized with the mCherry signal. This indicates a local accumulation of Ca^{2+} in regions with a high number of bacteria (Figures 1C and S1). Biofilms grown in these conditions also appeared opaque white, strongly suggesting that the P-Ca 10:10 growth condition favors calcium-based mineral precipitation in the biofilm.[37−39]

Mineralization Localizes Close to the Biofilm Interfaces and Involves Both Matrix and Bacteria Calcification. As fluorescence microscopy suggested nonuniform biofilm mineralization (Figure 1C), X-ray microtomography and cryo-FIB-SEM experiments were conducted to locate the minerals in the biofilm at different scales and in three dimensions (Figure 2). Microtomography was performed

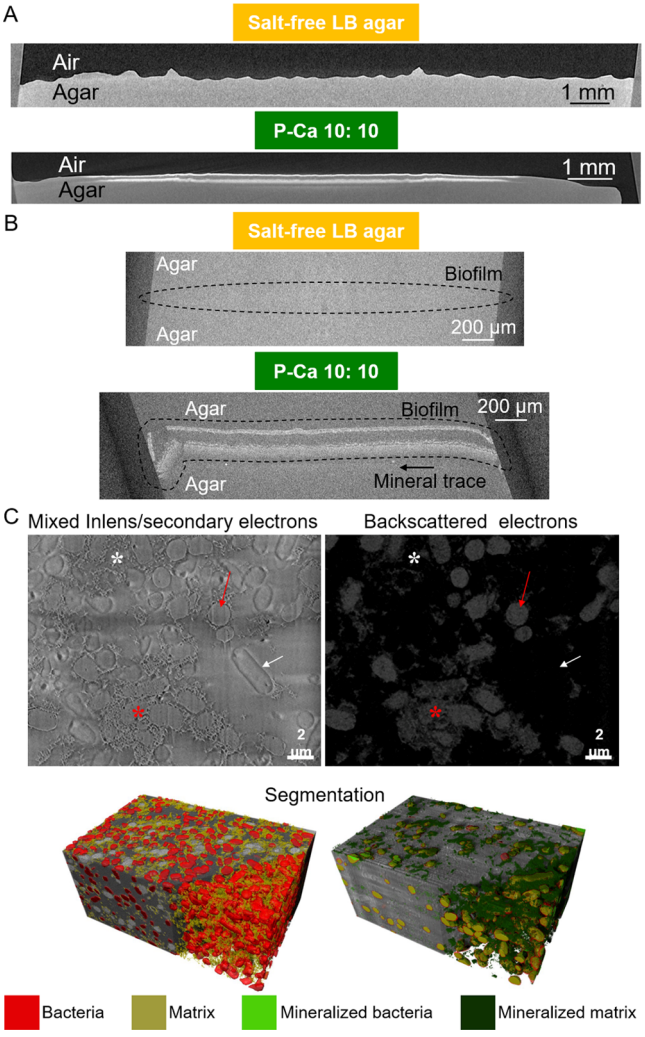

Figure 2. Precipitate location at different length scales. (A) Microtomography of biofilm cross sections. Biofilms were grown on salt-free LB agar and P-Ca 10:10 and fixed prior to the measurement. (B) Microtomography in the central region (1.5 mm diameter) of a biofilm grown on P-Ca 10:10. The sample was stabilized by pouring another agar layer on top of the biofilm. (C) Cryo-FIB-SEM analysis of a biofilm grown on P-Ca 10:10. Top: mixed Inlens and secondary electron image, revealing the structure due to differences in the local surface potential (left) and backscattered electron image, showing different densities (right). Arrows highlight mineralized (red) and unmineralized (white) bacteria, visible with the mixed Inlens/secondary electron detector. Bacteria loaded with denser particles (higher atomic number) provide a brighter contrast with the BSE detector. Stars show mineralized (red) and unmineralized (white) portions of the matrix. Bottom: Combining information from the backscattered and mixed Inlens/secondary electrons, it is possible to segment the sample and visualize all structures in three-dimensional (3D). On the left, unmineralized bacteria and matrix are highlighted, whereas, on the right, we show mineralized matrix and bacteria (see also Video S2).

https://doi.org/10.1021/acs.chemmater.2c02969
Chem. Mater. 2023, 35, 2762−2772

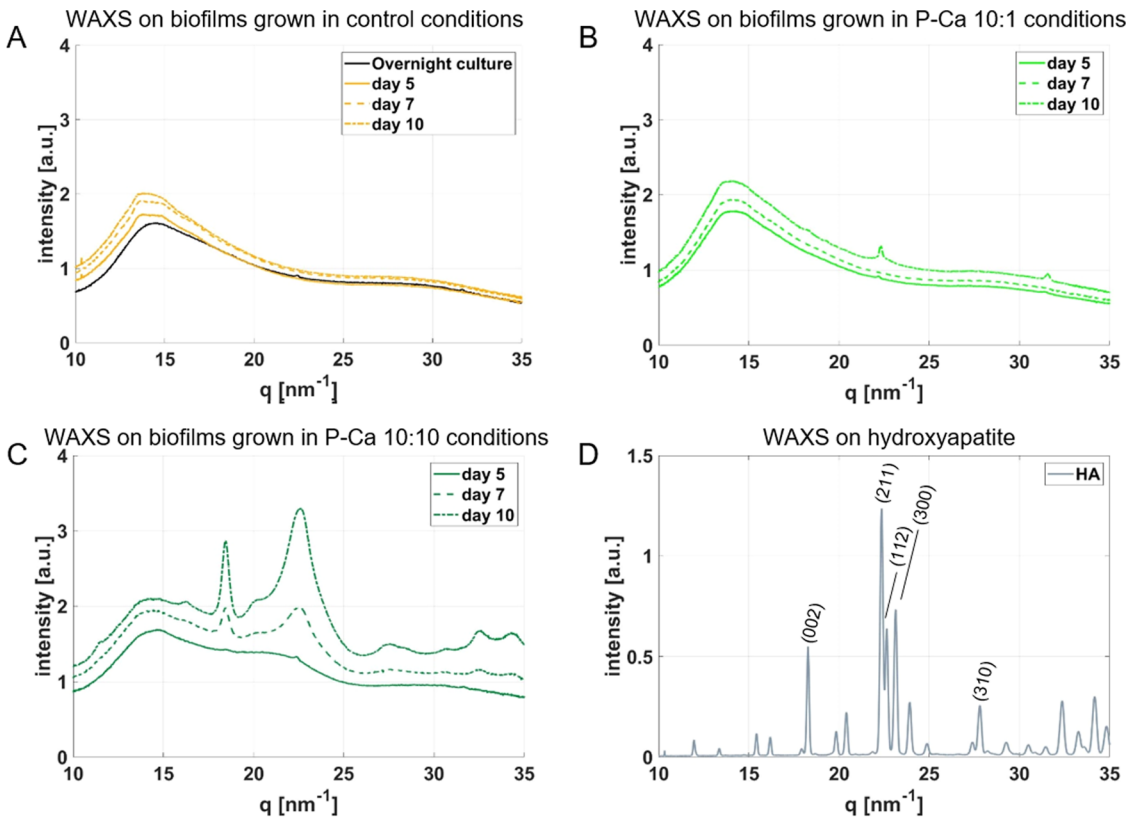

E

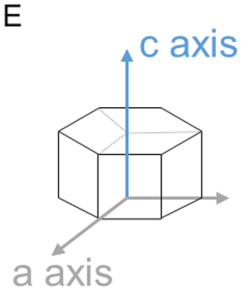

Peaks	Growth time	Particle size estimation	
		P-Ca 10:1 (nm)	P-Ca 10:10 (nm)
002 (c axis)	Day 5	nd	11.92 ± 0.55
	Day 7	nd	12.14 ± 0.15
	Day 10	17.68 ± 0.80	12.25 ± 0.08
310 (estimation of a axis)	Day 5	nd	nd
	Day 7	nd	5.98 ± 0.19
	Day 10	2.99 ± 0.07	5.48 ± 0.05

Figure 3. Mineral phase characterization through WAXS analysis. (A–C) WAXS diagrams of lyophilized biofilms after 5, 7, and 10 days of culture: (A) biofilms grown on salt-free agar; (B) biofilms grown on P-Ca 10:1 agar; and (C) biofilms grown on P-Ca 10:10 agar. (D) Diagram of HA as a reference. (E) Scheme of an HA crystal and estimation of HA particle size, using the 002 and 310 peaks ("nd" stands for "not detectable"). Data are shown as mean ± standard error of the mean (n = 12).

with fixed biofilms that were grown for 10 days on salt-free LB agar and on P-Ca 10:10 substrates. Biofilms grown on salt-free LB agar did not show a contrast difference with respect to the agar. On the contrary, P-Ca 10:10 biofilms clearly showed regions of higher gray levels close to the biofilm–air and biofilm–agar interfaces, which indicated a higher concentration of elements absorbing X-rays efficiently due to the high atomic number (like calcium). These regions were separated by a 50 μm thick layer within the biofilm that shows a lower degree of mineralization (Figure 2A).

To achieve higher resolution, we prepared biofilm samples of smaller volume. To stabilize the structure during sample preparation, a layer of agar was added on top of the biofilm. After solidification, a small cylinder (1.5 mm in diameter; 2 mm in thickness) was punched out of the central mineralized region. Biofilms grown on salt-free LB agar show little contrast differences with respect to the two layers of agar. This indicates that the thin layer at the interface between the biofilm and air in lower resolution microtomography (Figure 2A) is an artifact due to the density mismatch between the biofilm and the air. Microtomography of the P-Ca 10:10 sample revealed that the mineralized layer at the biofilm–agar interface was thicker than the layer at the biofilm–air interface (Figure 2B). The brittle fractures of these two layers, which most probably occurred when punching out the sample, indicated a radical change of biofilm material properties (e.g., toughness) upon mineralization (Figure 2B, left side). These data also confirmed that the mineralized layer at the biofilm–air interface was not a measurement artifact due to the density mismatch at the air interface. Moreover, the higher resolution achieved for this sample revealed a light trace of higher gray levels within the agar substrate that correlated with the observation of white

https://doi.org/10.1021/acs.chemmater.2c02969
Chem. Mater. 2023, 35, 2762–2772

traces in the agar after removing the biofilms from the substrate for further processing (e.g., for weighing) (Figure 2B, black arrow). The presence of minerals in the agar substrate indicated that the biofilms are also able to induce changes leading to mineralization in their surroundings.

Cryo-FIB-SEM provides resolution at the nanometer length scale and allows the visualization of individual bacteria and their surrounding matrix in a close to native state. After 10 days of growth in P-Ca 10:10 conditions, samples of approximately 1.5 mm in diameter were punched out from the central region of a biofilm containing precipitates. Cryo-FIB-SEM was used in the dual channel mode, allowing the simultaneous image acquisition from both a mixed Inlens/secondary electron detector as well as a backscattered electron detector (Figure 2C). The mixed Inlens/secondary electron detector allowed the identification of rod-like bacteria as well as the surrounding fibrous matrix. The backscattered detector revealed bright mineralized regions while unmineralized areas appeared dark. Taken together, these images show that, in some cases, minerals completely encapsulated and filled the bacteria (Figure 2C, red arrows), while other bacteria remained completely unmineralized (Figure 2C, white arrows). The fibrous matrix was easily distinguished in the mixed Inlens/secondary electron images. When viewed with the backscattered electron detector, the matrix also showed local differences in mineralization (Figure 2C). To distinguish and quantify the different regions in 3D (e.g., mineralized and unmineralized bacteria, mineralized and unmineralized matrix), the volume was segmented (Figure 2C, Video S2). Video S2 shows some clusters of mineralized bacteria surrounded by the mineralized matrix.

The segmentation of two stacks obtained by cryo-FIB-SEM enabled the semiquantitative analysis of about 4887 μm^3 of mineralized biofilm in total. The details of the quantification are presented in Table S3 and Figure S4. Minerals represent about 11% of the total volume probed and 40% of this mineral phase is found in the matrix, while 60% is found in the bacteria. Moreover, mineralization occurred in about 23% of the bacteria and half of them got at least 70% of their volume filled with minerals (see the histogram, S4). Interestingly, mineralized bacteria are on average 78% larger than unmineralized bacteria. This suggests that the mineralization induces significant deformations in the bacteria and/or most probably calcifies part of the organelles. We thus expect mineralization to critically impair bacteria viability. In the extracellular matrix, 46% of the fibrous material is mineralized, which is expected to induce significant changes of the material properties both at the molecular and macroscopic scales.

Minerals in *E. coli* Biofilms Precipitate in the Form of Hydroxyapatite. X-ray powder diffractometry (XRD) was conducted on fixed and freeze-dried biofilms to confirm the presence of minerals and identify their phase. This preparation enabled a systematic and high-throughput analysis. We initially measured biofilms grown in control (salt-free LB agar) and P-Ca 10:10 conditions, using an in-house diffractometer (Bruker D8). Biofilms grown in P-Ca 10:10 conditions showed peaks at q-values around 18 and 22.50 nm^{-1} (Figure S5A). Additionally, we analyzed the residual white stain in the agar, left by the mineralized biofilms after removing them from the surface (Figure S5B) as the microtomography analysis (Figure 2B) suggested mineral precipitation in this region. Agar samples were prepared in the same way as biofilms and revealed peaks similar to those obtained in the mineralized biofilms. No scattering peaks were detected in salt-free LB agar and in P-Ca 10:10 agar sampled in a region that showed no white stain (Figure S5B). The absence of mineral-related peaks in the agar media and in the biofilms grown in control conditions suggests that spontaneous precipitation is absent and that biofilm fixation does not induce mineralization. To differentiate the contribution of the two mineral precursors, we grew biofilms on salt-free LB agar with either 10 mM β-glycerophosphate (P-10) or 10 mM $CaCl_2$ (Ca-10). The XRD results (Figure S6) show that the sole presence of organic phosphoesters is not enough to induce mineral precipitation, whereas the presence of $CaCl_2$ induces minimal precipitation. This is likely due to the presence of phosphate-containing molecules in the yeast extract used as a nutrient in salt-free agar (Figure S6C).

More thorough analyses of the lyophilized biofilm powders were performed using synchrotron radiation in a wide-angle X-ray scattering (WAXS) setting (Figure 3). Biofilms cultivated on salt-free LB agar presented a broad single peak around q = 14 nm^{-1}, similar to a freeze-dried overnight culture containing bacteria only (Figure 3A). Biofilms cultivated in the presence of β-glycerophosphate and Ca^{2+} ions showed diffraction peaks typical for mineralization, depending on their respective growth stage. At a low calcium concentration (P-Ca 10:1, Figure 3B), peaks at q = 22.33 nm^{-1} and at q = 32.38 nm^{-1} were visible only starting from day 10. The first peak can be traced back to the 211, 112, and 300 peak family of HA (Figure 3D). At a high calcium concentration (P-Ca 10:10, Figure 3C), these peaks sharpened from day 5 to day 10, indicating crystal growth. Additionally, peaks around q = 18.10 and 27.85 nm^{-1} were detected. These correspond to the 002 and 310 reflection planes of a reference HA powder (Sigma-Aldrich) (Figure 3C). The match between the peaks observed in the biofilm and in the reference HA powder proves the colocalization of P and Ca elements in the form of HA crystals.

The Scherrer equation[40] enables us to estimate the crystal particle dimensions perpendicular to the corresponding planes (Figure 3E). Biofilms grown in P-Ca 10:10 conditions presented crystals with a dimension of about 12 nm along the c-axis (peak 002, Figure 3E). Even though the average dimension increased over time, growth was not statistically significant ($p > 0.01$ under the hypothesis of normal distribution with a one-way analysis of variance (ANOVA) test, n = 12). The 310 peak allowed us to estimate the dimension of the diagonal of the hexagonal crystal base to range between 5.5 and 6 nm. Just as for the 211, 112, and 300 peak family, the 002 and 310 peaks were only detectable after 10 days when biofilms were grown in P-Ca 1:10 conditions. In these conditions, these peaks represented significantly longer yet thinner particles of about 17.7 nm length and 3 nm base diagonal. The biofilm growth conditions thus seemed to influence the morphology of the resulting hydroxyapatite particles.

ALP Promotes Hydroxyapatite Deposition in *E. coli* Biofilms. Inspired by the mechanisms of hydroxyapatite mineralization involved in bone tissues, we then tested the hypothesis that mineralization is mediated by bacterial ALP. We implemented two strategies: (1) cultivating biofilms on a substrate containing the weak ALP inhibitor L-glutathione ($IC_{50} \sim 2$ mM)[41] and (2) testing the activity of the enzyme alone on P-Ca 10:10 agar plates. The inhibitor L-glutathione[41] was added in the P-Ca 10:10 agar, and biofilms were grown under the same conditions as in the previous experiments. To ensure that the ALP inhibitor did not interfere with biofilm

https://doi.org/10.1021/acs.chemmater.2c02969
Chem. Mater. 2023, 35, 2762−2772

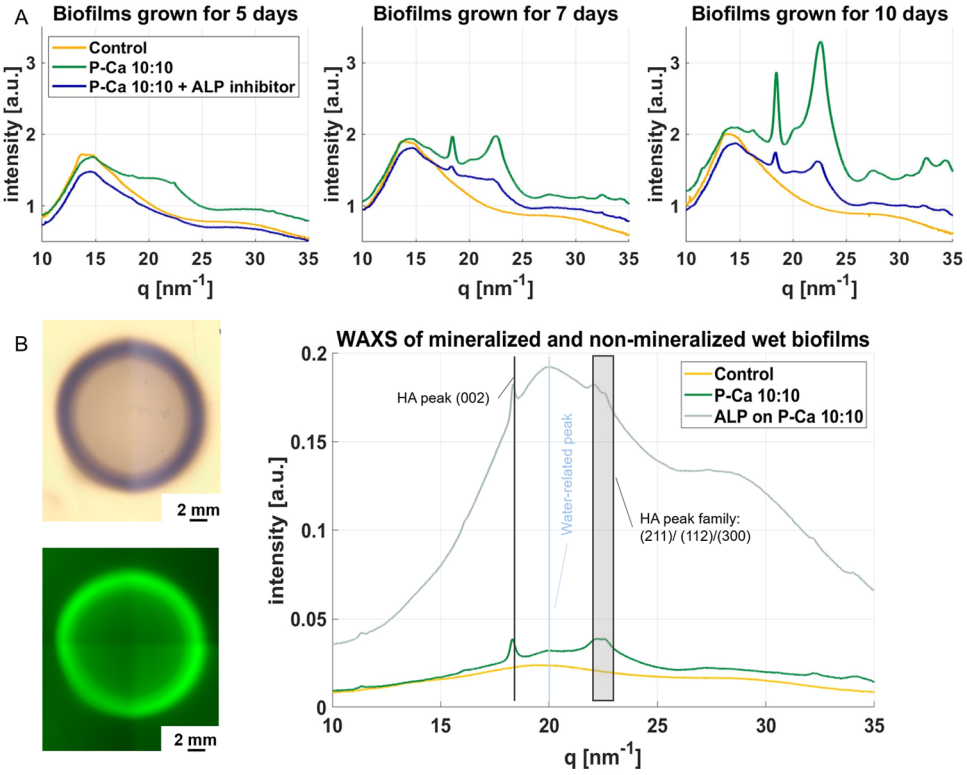

Figure 4. ALP and biofilm mineralization. (A) WAXS diagrams of freeze-dried biofilms cultivated on LB agar, on P-Ca 10:10 agar and on P-Ca 10:10 agar supplemented with the ALP inhibitor. (B) Mineralization induced by an ALP solution spotted onto P-Ca 10:10 agar. Left: Stereomicroscopy showing reflected light (top) and Calcein fluorescence (bottom). Right: WAXS diagrams of an area, where a droplet of bacterial ALP solution was deposited on P-Ca 10:10 agar and hydrated biofilms grown on P-Ca 10:10 agar and salt-free LB agar.

growth, we measured the diameter of P-Ca 10:10 + L-glutathione biofilms and they did not show a significant difference with respect to the control condition (Figure S7). Comparing WAXS diagrams of biofilms grown in P-Ca 10:10 conditions with and without inhibitor showed a delayed appearance of the HA peaks 002 and 310 in the presence of an inhibitor. In the absence of an inhibitor, peak 002 appeared very broad from day 5 and became sharper over time (Figure 4A, green lines). Peak 310 followed the same trend yet started to be detectable from day 7. When the inhibitor was present (Figure 4A), both peaks 002 and 310 were less pronounced and only started appearing at day 7. WAXS thus confirms that mineral precipitation in the biofilms is delayed in the presence of a weak ALP inhibitor. Yet, a few HA crystals were still detectable in biofilms grown for 10 days with the inhibitor. These crystals showed a *c*-axis of 13.05 ± 0.14 nm (mean ± standard error of the mean) and were thus significantly longer than the crystals found in biofilms grown without inhibitor.

To test ALP activity independent from the other biofilm components, a droplet of purified ALP was deposited on P-Ca 10:10 agar containing Calcein. After overnight incubation at 28 °C, the droplet left a marked dark trace with high Calcein fluorescence, indicating a higher local concentration of calcium (Figure 4B, left). A comparison of the WAXS results of the hydrated material with a mineralized biofilm grown in P-Ca 10:10 conditions (not lyophilized) revealed the typical peaks at q = 18.1 nm^{-1}, 22.5 nm^{-1}, and (quite shallow) 27.85 nm^{-1} (Figure 4B). This shows that in the presence of calcium and β-glycerophosphate, ALP alone can induce the precipitation of HA minerals. As minerals are also found in native (wet) biofilms, these results confirm that the minerals detected in the freeze-dried biofilms were not artifacts from sample preparation. These two independent experiments thus strongly suggest that bacterial ALP is essential and sufficient for biomineralization when *E. coli* biofilms are grown in the presence of calcium ions and β-glycerophosphate.

Additional experiments involving a fixed biofilm material incubated on the mineralizing medium for 10 days revealed that living bacteria are not necessary to induce mineralization, as detected by Calcein staining and XRD analysis (Figure S9). However, further mineralization tests performed in liquid mineralizing medium and combined with measurements of ALP activity using p-nitrophenyl phosphate (pNPP)[24] showed that a critical amount of active ALP is necessary to induce HA crystal formation in the presence of the P-Ca 10:10 medium (Table S10). While the overnight culture of a single colony of *E. coli* bacteria in mineralizing media revealed ALP activity and HA mineralization, the filtered medium from the same overnight culture showed almost neither ALP activity nor mineralization. These results not only indicate that the ALP enzyme is intracellular but also that the pNPP substrate used to detect ALP activity is able to cross the outer membrane of the bacteria, thereby suggesting that the β-glycerophosphate substrate could potentially follow a similar path.

DISCUSSION AND CONCLUSIONS

This work shows that *E. coli* biofilms grown on a solid medium induce the precipitation of hydroxyapatite (HA) particles in the presence of calcium ions and organic phosphoesters. Our results also suggest that this biomineralization process is actively supported by bacterial alkaline phosphatase (ALP). Previous biogeological work has shown that individual *E. coli*

https://doi.org/10.1021/acs.chemmater.2c02969
Chem. Mater. 2023, 35, 2762−2772

bacteria can precipitate HA minerals when incubated in a solution of calcium ions and organic phosphoesters in the absence of nutrients.[31] This biomineralization process was particularly effective in *E. coli* cells overexpressing PhoA in the periplasm or in the cytoplasm. Most interestingly, mineral accumulation occurred independent of cellular PhoA localization, suggesting that PhoA and inorganic phosphate are secreted into the extracellular space[31] or that Ca^{2+} and the organic phosphoester can enter the periplasm (as demonstrated for pNPP in liquid culture, Table S10). Based on these observations, we implemented similar mineralization conditions in our *E. coli* biofilm growth protocol and tested two concentrations of precursors in the range of human physiological conditions (Figure 1A). We showed that *E. coli* biofilm mineralization occurs in conditions where the concentrations of these precursors match those of the saliva (P-Ca 10:1)[20,36] but with a time delay compared to conditions with higher concentrations (P-Ca 10:10). As human plasma contains on average 2.5 mM calcium,[42] our experimental model is physiologically relevant and the P-Ca 10:10 condition can be representative of pathological situations, where calcium ions tend to accumulate in given locations.[43] Calcium has been shown to influence biofilm formation in many different ways depending on the bacterial strain. Calcium is essential to form the calcite scaffold sustaining *B. subtilis* biofilms,[44] calcium-regulated sensors and regulators are involved in the expression of the polysaccharide matrix in *Vibrio cholerae* biofilms,[45] and calcium favors the expression and the stability of the *Pseudomonas aeruginosa* biofilm alginate matrix, thereby increasing virulence.[46] Here, we focus on calcium as a precursor involved in *E. coli* biofilm mineralization.

The primary biological function of ALP is to mediate the availability of inorganic phosphate for metabolic processes. In prokaryotes, ALP is expressed when the concentration of inorganic phosphate is low, enabling the dephosphorylation of a wide range of organic phosphomonoesters, including phosphorylated proteins, lipids, carbohydrates, and nucleic acids.[47] In particular, *E. coli* was shown to increase ALP production by several hundred times in such conditions.[48] While ALP plays an essential role in phosphate metabolism, its role in biofilm formation (e.g., matrix synthesis) and mineralization has not yet been investigated.[32] Prokaryotic ALP dephosphorylates teichoic acid, a molecule that plays a key role for bacterial colonization on artificial surfaces. More importantly, dephosphorylation of organic phosphoesters and polyphosphates liberates phosphate ions that may lead to supersaturation in the presence of Ca^{2+} ions. Purified bacterial ALP deposited on the mineralizing agar medium used for biofilm growth (Figure 4B) induced HA mineralization similar to the addition of ALP to a solution of calcium ions and organic source of phosphates.[31] This suggests a critical role of the enzyme in bacteria and biofilm mineralization, as supported by the delay of mineral formation when the ALP inhibitor was added (Figure 4A).

Whether the formation of calcium phosphate minerals is favorable or not to the bacterial community is not clear and may depend on the physiological context. In the present experimental conditions, mineralized biofilms are smaller and lighter (Figure 1B), and the cryo-FIB-SEM images show that most of mineralized bacteria have more than half of their volume filled with hydroxyapatite (Figure 2C). Yet, while mineralization causes the death of a large fraction of bacteria,[31] the resulting composite material may offer protection to the small number of surviving bacteria and, overall, to the whole community. With this in mind, the less mineralized layer in between the mineralized top and bottom layers could become an environment, where bacteria are protected from their surroundings (Figure 2A,B). The mineralized layers could block the diffusion of mineralization precursors and prevent mineralization of the entire biofilm and its bacterial population. From a population point of view, it could thus be worth the sacrifice of a fraction of bacteria through partial or complete mineralization. Such social behavior has already been described for bacterial communities in different contexts.[49,50] Note that in some contexts, bacterial sacrifice consists in entering a dormant state, also called "viable but nonculturable state"; however, the cryo-FIB-SEM images and analyses suggest a significant destruction of the intracellular space that would compromise the future resuscitation of the mineralized bacteria (Figure 2C, Video S2).

There is no obvious correlation between the appearance of these layers and the cross-sectional structure of nonmineralized biofilms produced by the same bacteria.[51] It is thus not clear if and how this layered geometry is collectively controlled by the bacteria or if it results from physicochemical phenomena that involve a combination of diffusion and phase transitions. Indeed, layered periodic patterns of HA minerals, akin to Liesegang rings, spontaneously form in agar in the presence of inorganic calcium and phosphate ion sources.[52] Once phosphate ions are enzymatically released from β-glycerophosphate, our experimental conditions may resemble those of this study. This diffusion-based phenomenon may then explain the layered mineralization pattern in the biofilms and also the mineralization layer detected within the agar substrate, i.e., relatively far away from the bacteria (Figure 2B).

The following remains an open question: which key player is able to diffuse in the biofilm environment? Considering the control experiment shown in Table S10, it appears likely that β-glycerophosphate is taken up by the bacteria into the periplasmic space. Intracellular localization of phosphate and Ca^{2+} would then explain the observed mineralization of bacteria. This does, however, not explain matrix mineralization. Even though no ALP activity was detected in the medium of liquid cultures, it cannot be excluded that the enzyme will be secreted in a biofilm environment, where the bacteria are in a different metabolic state. This study further shows that alive bacteria are not necessary to induce HA mineralization in the presence of calcium ions and organic source of phosphates (Figures 4 and S9), suggesting a passive uptake or secretion mechanism. These observations not only point in the direction of ALP having a prominent role in HA mineralization in *E. coli* biofilms but they also highlight that further investigations are required to clarify the mechanisms that determine the patterns of mineralization in biofilms.

Similar to what is known about the role of collagen in bone apatite formation,[53] biofilm matrix fibers may be involved in the nucleation of the mineral crystals due to favored interactions between ionic precursors and charged amino acids.[54] In particular, curli fibers may serve as a scaffold to mediate HA mineralization as shown by in vitro studies with purified curli fibers.[55] Moreover, the *E. coli* biofilm matrix may also influence the growth and morphology of the HA crystals like the *B. subtilis* biofilm matrix was shown to influence the formation of calcium carbonate crystals.[56] Applying the strategy presented in this work to *E. coli* strains producing extracellular matrices of different compositions would enable

https://doi.org/10.1021/acs.chemmater.2c02969
Chem. Mater. 2023, 35, 2762−2772

us to assess the role of the organic microbial matrix on the nanoscopic properties of the minerals formed and on the resulting macroscopic properties of the biofilm.[57] For example, such a study performed on uropathogenic *E. coli* could have interesting implications for clarifying the origins of kidney stones.[58,59]

Altogether, the present work provides fundamental knowledge on biomineralization in microbial tissues as well as a platform to investigate biofilm calcification in a controlled environment that can be representative of physiological conditions. Insights into the interplay between metabolic state, biofilm structure, and the accumulation of mineralization precursors will benefit not only the prevention of biofilm mineralization in the context of pathologies (dental calculus, kidney stones)[9,10,18] but also the engineering of biofilm-based living materials. Of particular interest are biofilm-based composites that are currently investigated as a potential source of sustainable materials with versatile properties adapted to various applications, such as self-repairing concrete and photosynthetic living materials.[17,60,61]

MATERIALS AND METHODS

Mineralization Medium and Biofilm Inoculation. *E. coli* biofilms were cultivated at the solid−air interface using tailored agar plates (15 cm diameter). Salt-free LB agar (Luria/Miller) plates (control medium) were prepared with 1.8% w/v bacteriological grade agar−agar (Roth 2266), 1% w/v tryptone (Roth 8952), and 0.5% w/v yeast extract (Roth 2363). For the mineralizing media, calcium ions were added in the form of $CaCl_2$ (Sigma-Aldrich 223506). Sodium ß-glycerophosphate (Sigma-Aldrich 35675) was added to the LB agar substrate as an organic source of phosphates. $CaCl_2$ and sodium ß-glycerophosphate were sterile-filtered (0.22 μm) and added to the autoclaved and still liquid salt-free LB agar to reach a final concentration of 10 mM ß-glycerophosphate and 1 or 10 mM $CaCl_2$. These conditions were, respectively, named P-Ca 10:1 and P-Ca 10:10. Measuring the osmolarities of liquid versions of the salt-free LB medium (89 mOsm/kg) and the P-Ca 10:10 medium (137 mOsm/kg) enabled to exclude that bacteria experienced an osmotic shock, considering the much higher osmolarity of the regular LB medium used for the overnight cultures (411 mOsm/kg).

If calcium staining was required, a Calcein Green (Merck KGaa, 102315) stock solution (1 mM in 10 mM NaOH) was also added to the liquid LB agar to reach a final concentration of 4 μM. Note that this type of Calcein reports extracellular calcium. For the cultures with the ALP inhibitor, a sterile-filtered L-glutathione (reduced, Sigma-Aldrich G4251) solution was added to the liquid agar to a final concentration of 20 mM.

The *E. coli* K-12 strain W3110 was chosen as a well-characterized model strain.[33] To visualize the bacterial cells using fluorescence stereomicroscopy, the bacteria were transformed with the plasmid pMP7604 (TetR; obtained from Guido V. Bloemberg, University of Zurich) that carries the gene for the fluorescent protein mCherry.[62] The gene is under control of the strong *tac* promotor, and the repressor was removed to allow for constitutive and strong expression of mCherry. It has been shown that this plasmid is stable and maintained in *E. coli* for at least 30 generations without selection pressure.[62] This plasmid is thus an ideal marker for fluorescently labeling *E. coli* bacteria in a biofilm, avoiding the need for antibiotics.

In each plate, biofilms were inoculated with an array of 9 droplets, each using 5 μL of bacterial suspension (OD_{600} ∼ 5.0). The suspension was obtained from a single *E. coli* microcolony that was grown overnight in LB medium (Luria/Miller) (Roth X968) at 37 °C and 250 rpm. After seeding, the droplets were left to dry and the inoculated dishes were incubated at 28 °C for 5, 7, and 10 days. For the seeding on the dishes with the inhibitor, the LB medium for the overnight culture was also supplemented with 5 mM L-glutathione.

Apart from those used for stereomicroscopy, all biofilms were fixed with 4% paraformaldehyde (PFA, Bioster Ar106) in phosphate-buffered saline (PBS, Sigma-Aldrich P4417). The fixing solution was spread on the edge of each biofilm and left to react for 15 min. The excess solution was removed and substituted with fresh PFA. After another 15 min, the excess was again removed and the entire biofilm was covered with the fixing solution. The solution was left in contact with the biofilm for 2 h. The excess was then removed and the biofilms were rinsed with the aforementioned PBS solution.

Cryo-FIB-SEM and Serial Surface View (SSV) Imaging. Biofilms were grown for 10 days at 28 °C and fixed. Samples were collected from one complete biofilm, puncturing the central mineralized region at different locations with a disposable antistatic microspatula with a diameter of 2 mm (VWR International, Radnor, PA). The samples were then sandwiched between two discs of 3 mm diameter, type A and type B gold-coated copper freezer hats (BALTIC preparation, Wetter, Germany), allowing an inner cavity of 0.5 mm in thickness with the addition of 10% dextran as a cryoprotectant and cryoimmobilized in a HPM100 high-pressure freezing machine (Leica Microsystems, Vienna, Austria). The sample carriers containing the samples were mounted on a cryo sample holder in the Leica EM VCM loading station (Leica Microsystems, Vienna, Austria) at liquid nitrogen temperature. The sample holder was then transferred using a VCT500 shuttle for freeze-fracture and sputter coating (ACE600, Leica Microsystems, Vienna, Austria). After freeze-fracture, the exposed samples were sputter-coated with a platinum layer (thickness 8 nm). Finally, the samples were transferred to a Zeiss Crossbeam 540 microscope (Zeiss Microscopy GmbH, Oberkochen, Germany) using the VCT500 shuttle. Throughout the analysis, the biofilm samples were kept at a temperature below −145 °C.

Cryo-FIB-SEM serial surface view imaging was performed using a Zeiss Crossbeam 540 dual-beam FIB-SEM in cryo-conditions (Zeiss Microscopy GmbH, Oberkochen, Germany). Three samples were used, resulting in three different stacks. The samples were elevated to a height of 5.1 mm, which corresponds to the coincident point of the two beams, and tilted to 54°. A trench of 20 μm length and 60 μm width was milled at 30 nA. The exposed surface was polished with a lower ion beam current (1.5 nA). The electron beam was then focused on the polished exposed tissue at 1.3 keV and 25 pA for stack 1 and 1.8 keV and 50 pA for stacks 2 and 3. Images were sequentially collected using the "slice and view" protocol. The pixel size of the image prior to data collection was set at 8 nm for one stack and 10 nm for the two other stacks in the x and y directions. The slice thickness (z direction) was set to maintain an isometric voxel size, namely, 8 nm for the first stack and 10 nm for the two others. All stacks were acquired with an image resolution of 2048 × 1536 pixels and in 8-bit grayscale. The first stack comprises 2082 slices, the second, 1340 slices, and the third one, 1476 slices. For each stack, the dual channel option was enabled to simultaneously acquire images from the mixed Inlens/secondary electron (SE) detector and the backscattered electron (BSE) detector.

Image Processing. Stack alignment, image processing, segmentation, and video generation were performed using Dragonfly software, version 2021.1 (Object Research Systems (ORS) Inc, Montreal, Canada). BSE and mixed Inlens/SE images were first automatically aligned using the sum of squared difference (SSD) method available in the slice registration panel. Curtaining artifacts produced by the beam during the milling process were corrected using a vertical destriping filter. A gradient domain fusion filter was applied only to the mixed Inlens/SE images in order to attenuate the discontinuities in the illumination from registered image stacks in the z direction. Finally, the contrast was improved and the noise was reduced using a convolution filter in all images. The segmentation was performed with the deep learning module in Dragonfly software. For training, 20 slices were used for each data set, followed by a manual refinement using the 'brush' tool.

Detection of Calcium Phosphate. *Fluorescence Stereomicroscopy.* After 5, 7, or 10 days of growth, pictures were taken from live biofilms with an AxioZoomV.16 fluorescence microscope (Zeiss,

https://doi.org/10.1021/acs.chemmater.2c02969
Chem. Mater. 2023, 35, 2762−2772

Germany). Images were taken in reflected light mode with an exposure time of 15 ms. The fluorescence signal from Calcein Green was collected with a 38 HE green fluorescent protein filter cube with the following specifications (excitation: 470/40 nm; beam splitter: FT 495 nm; emission 525/50 nm). The exposure time was 100 ms. mCherry fluorescence was detected using a 63 He red fluorescent protein filter cube (excitation: 572/25 nm; beam splitter: FT 590 nm; emission: 629/62 nm). The exposure time was 500 ms.

Biofilm diameters were estimated using custom-written MATLAB codes (Matlab 9.7.0 R2019b, MathWorks, Natick, MA). For the diameter calculation, the images taken in reflected light mode were converted to grayscale. With the function "edge," we obtained skeletonized pictures and, after removing the noise with the function "bwareaopen," we interpolated the remaining points with a circle and calculated the diameter of the circle.

Microtomography. After 10 days of growth, fixed biofilms were cut out from the cultivation dishes using the upper part of disposable plastic Pasteur pipettes (12 mm diameter). The samples were kept sealed to avoid water evaporation. For both salt-free LB agar and the P-Ca 10:10 biofilms, a similar procedure was replicated in the center of the biofilms but using disposable antistatic microspatulae with a diameter of 2 mm (VWR International, Radnor, PA). Samples were imaged using an X-ray microtomography scanner (RX Solutions EasyTom160/150 tomographic unit) with a voxel size of 8 μm at 70 kV and 130 μA for the larger samples and a voxel size of 1.65 μm at 80 kV and 69 μA for the smaller samples.

Identification of the Calcium Phosphate Phase. To identify the mineral phase, we processed the biofilms to obtain a powder. After fixation, biofilms underwent freeze-drying in a lyophilizer (Lyo α 1-2 LD; Martin Christ, Osterode am Harz, Germany) (pressure: 0.63 bar, temperature: −25 °C, overnight). Once freeze-dried, the powders were milled with an agate mortar to obtain a finer powder.

Wide-Angle X-ray Scattering (WAXS). Powdered samples were filled into a 2 mm Teflon sample holder with multiple holes of 5 mm diameter. The samples were overlaid with a Kapton film on both sides. Small-angle/wide-angle X-ray scattering (SAXS/WAXS) measurements were performed at the μSpot beamline at the BESSY II synchrotron (Helmholtz Zentrum für Materialien und Energie, Berlin, Germany).[63] The complete diagrams are shown in Figure S4. The measurements were carried out using a B4C/Mo multilayer (2 nm period) monochromator and an energy of 15 keV. A sequence of pinholes was used to select a 30 × 30 μm^2 spot size. Data were normalized over the primary beam intensity, and the background was subtracted. Transmission through the sample was calculated from an X-ray fluorescence signal collected from a lead beam stop using a RAYSPEC Sirius SD-E65133-BE-INC detector. The detector was equipped with an 8 μm beryllium window, where the primary beam intensity was monitored using an ion chamber. Scattering data were collected with an Eiger 9M detector with a 75 × 75 μm^2 pixel area. For each sample, four spots were measured and diffraction patterns were collected with an exposure time of 15 s. Further data processing and reduction were done using the directly programmable data analysis kit (DPDAK).[64] Diffraction patterns were radially integrated, and the scattered intensity $I(q)$ was calculated as a function of the momentum transfer q, defined as

$$q = \frac{4\pi}{\lambda}\sin\left(\frac{\theta}{2}\right) \quad (1)$$

where λ and θ denote the photon wavelength and the scattering angle, respectively. The sample-to-detector distance was set to approximately 330 mm ($0.1 < q < 30$ nm^{-1}) and calibrated by using quartz powder. Data were analyzed with in-house Python-based software (Python 3.8.8).

Mineralization in the Presence of Purified ALP. ALP (100U) from *E. coli* (Sigma-Aldrich P5931, lot# 039M4019V) was dissolved in glycine buffer (0.1 M glycine/NaOH pH 10.4, 1 mM $MgCl_2$, 1 mM $ZnCl_2$). A droplet of this bacterial ALP solution (100 μL; 20 U/mL) was deposited on P-Ca 10:10 agar containing Calcein Green and incubated overnight at 28 °C. Samples were analyzed by stereomicroscopy and scattering experiments similar to the biofilms.

■ ASSOCIATED CONTENT

Data Availability Statement

Data and analysis tools are available upon request to the corresponding author.

Supporting Information

The Supporting Information is available free of charge at https://pubs.acs.org/doi/10.1021/acs.chemmater.2c02969.

Stereomicroscopy from 3 to 10 days of growth; segmentation 3D reconstruction; low-resolution XRD diagrams and additional growth conditions; diameter of P-Ca 10:10 + ALP inhibitor biofilms; SAXS and WAXS complete diagrams; fixed biofilms on P-Ca 10:10 and salt-free LB agar; and ALP activity estimation and *E. coli* mineralizing behavior under various conditions (PDF)

Segmentation 3D reconstruction (MP4)

■ AUTHOR INFORMATION

Corresponding Author

Laura Zorzetto − *Department of Biomaterials, Max Planck Institute of Colloids and Interfaces, 14476 Potsdam, Germany;* orcid.org/0000-0003-3126-5741; Email: Laura.Zorzetto@mpikg.mpg.de

Authors

Ernesto Scoppola − *Department of Biomaterials, Max Planck Institute of Colloids and Interfaces, 14476 Potsdam, Germany;* orcid.org/0000-0002-6390-052X

Emeline Raguin − *Department of Biomaterials, Max Planck Institute of Colloids and Interfaces, 14476 Potsdam, Germany*

Kerstin G. Blank − *Mechano(bio)chemistry, Max Planck Institute of Colloids and Interfaces, 14476 Potsdam, Germany; Institute of Experimental Physics, Johannes Kepler University Linz, 4040 Linz, Austria;* orcid.org/0000-0001-5410-6984

Peter Fratzl − *Department of Biomaterials, Max Planck Institute of Colloids and Interfaces, 14476 Potsdam, Germany;* orcid.org/0000-0003-4437-7830

Cécile M. Bidan − *Department of Biomaterials, Max Planck Institute of Colloids and Interfaces, 14476 Potsdam, Germany;* orcid.org/0000-0002-6243-562X

Complete contact information is available at: https://pubs.acs.org/10.1021/acs.chemmater.2c02969

Author Contributions

This manuscript was written through contributions of all authors. All authors have given approval to the final version of the manuscript.

Funding

Open access funded by Max Planck Society.

Notes

The authors declare no competing financial interest.

■ ACKNOWLEDGMENTS

The authors thank Dr. Guido V. Bloemberg (University of Zurich) for the gift of the pMP7604 plasmid and Prof. Regine Hengge (Humboldt-Universität zu Berlin) for kindly providing *E. coli* strain W3110. L.Z. acknowledges Christine Pilz for teaching her microbiological laboratory techniques. They

thank Jeannette Steffen, Susann Weichold, and Clemens Schmitt for their help with sample preparation. They also thank Daniel Werner for collecting the microtomography data and Dr. Chenghao Li for the help provided calibrating the instruments at BESSY facilities. L.Z. acknowledges the research consortium of InterDent and the financial support of the German Research Foundation (Deutsche Forschungsgemeinschaft—DFG) DFG: FOR2804.

REFERENCES

(1) Madigan, M. T.; Bende, K. S.; Buckley, D. H.; Sattley, W. M. *Brock Biology of Microorganisms*, 15th ed.; Pearson Education Limited: London, 2015.
(2) Oppenheimer-Shaanan, Y.; Sibony-Nevo, O.; Bloom-Ackermann, Z.; Suissa, R.; Steinberg, N.; Kartvelishvily, E.; Brumfeld, V.; Kolodkin-Gal, I. Spatio-Temporal Assembly of Functional Mineral Scaffolds within Microbial Biofilm. *npj Biofilms Microbiomes* **2016**, *2*, 1−10.
(3) Mann, S. *Biomineralization: Principles and Concepts in Bioinorganic Materials Chemistry*; Oxford University Press: New York, NY, 2001.
(4) Decho, A. W. Overview of Biopolymer-Induced Mineralization: What Goes on in Biofilms? *Ecol. Eng.* **2010**, *36*, 137−144.
(5) Barabesi, C.; Galizzi, A.; Mastromei, G.; Rossi, M.; Tamburini, E.; Perito, B. *Bacillus subtilis* Gene Cluster Involved in Calcium Carbonate Biomineralization. *J. Bacteriol.* **2007**, *189*, 228−235.
(6) ten Cate, J. M. Biofilms, a New Approach to the Microbiology of Dental Plaque. *Odontology* **2006**, *94*, 1−9.
(7) Akcalı, A.; Lang, N. P. Dental Calculus: The Calcified Biofilm and Its Role in Disease Development. *Periodontology 2000* **2018**, *76*, 109−115.
(8) Schwaderer, A. L.; Wolfe, A. J. The Association between Bacteria and Urinary Stones. *Ann. Transl. Med.* **2017**, *5*, No. 32.
(9) Nguyen, P. Q.; Courchesne, N. M. D.; Duraj-Thatte, A.; Praveschotinunt, P.; Joshi, N. S. Engineered Living Materials: Prospects and Challenges for Using Biological Systems to Direct the Assembly of Smart Materials. *Adv. Mater.* **2018**, *30*, No. 1704847.
(10) Yu, K.; Spiesz, E. M.; Balasubramanian, S.; Schmieden, D. T.; Meyer, A. S.; Aubin-Tam, M. E. Scalable Bacterial Production of Moldable and Recyclable Biomineralized Cellulose with Tunable Mechanical Properties. *Cell Rep. Phys. Sci.* **2021**, *2*, No. 100464.
(11) Omelon, S.; Ariganello, M.; Bonucci, E.; Grynpas, M.; Nanci, A. A Review of Phosphate Mineral Nucleation in Biology and Geobiology. *Calcif. Tissue Int.* **2013**, *93*, 382−396.
(12) Coe, F. L.; Parks, J. H.; Asplin, J. R. The Pathogenesis and Treatment of Kidney Stones. *N. Engl. J. Med.* **1992**, *327*, 1141−1152.
(13) Borghi, L.; Guerra, A.; Meschi, T.; Briganti, A.; Schianchi, T.; Allegri, F.; Novarini, A. Relationship between Supersaturation and Calcium Oxalate Crystallization in Normals and Idiopathic Calcium Oxalate Stone Formers. *Kidney Int.* **1999**, *55*, 1041−1050.
(14) Curhan, G. C.; Willett, W. C.; Speizer, F. E.; Stampfer, M. J. Twenty-Four−Hour Urine Chemistries and the Risk of Kidney Stones among Women and Men. *Kidney Int.* **2001**, *59*, 2290−2298.
(15) Bazin, D.; Papoular, R. J.; Elkaim, E.; Weil, R.; Thiaudière, D.; Pisapia, C.; Ménez, B.; Hwang, N. S.; Tielens, F.; Livrozeth, M.; Bouderlique, E.; Haymann, J.-P.; Letavernier, E.; Hennet, L.; Frochoth, V.; Daudon, M. Whitlockite Structures in Kidney Stones Indicate Infectious Origin: A Scanning Electronmicroscopy and Synchrotron Radiation Investigation. *C. R. Chim.* **2021**, *25*, 1−12.
(16) Saw, J. J.; Sivaguru, M.; Wilson, E. M.; Dong, Y.; Sanford, R. A.; Fields, C. J.; Cregger, M. A.; Merkel, A. C.; Bruce, W. J.; Weber, J. R.; Lieske, J. C.; Krambeck, A. E.; Rivera, M. E.; Large, T.; Lange, D.; Bhattacharjee, A. S.; Romero, M. F.; Chia, N.; Fouke, B. W. In Vivo Entombment of Bacteria and Fungi during Calcium Oxalate, Brushite, and Struvite Urolithiasis. *Kidney360* **2021**, *2*, 298−311.
(17) Heveran, C. M.; Williams, S. L.; Qiu, J.; Artier, J.; Hubler, M. H.; Cook, S. M.; Cameron, J. C.; Srubar, W. V. Biomineralization and Successive Regeneration of Engineered Living Building Materials. *Matter* **2020**, *2*, 481−494.
(18) Wang, Y.; An, B.; Xue, B.; Pu, J.; Zhang, X.; Huang, Y.; Yu, Y.; Cao, Y.; Zhong, C. Living Materials Fabricated via Gradient Mineralization of Light-Inducible Biofilms. *Nat. Chem. Biol.* **2020**, *17*, 351−359.
(19) Fratzl, P.; Weinkamer, R. Nature's Hierarchical Materials. *Prog. Mater. Sci.* **2007**, *52*, 1263−1334.
(20) Lagerlöf, F. Effect of Flow Rate of PH on Calcium Phosphate Saturation in Human Parotid Saliva. *Caries Res.* **1983**, *17*, 403−411.
(21) Neuman, W.; Neuman, M. *The Chemical Dynamics of Bone Mineral*; University of Chicago Press: Chicago, 1958.
(22) Khongkhunthian, S.; Kongtawelert, P.; Ongchai, S.; Pothacharoen, P.; Sastraruji, T.; Jotikasthira, D.; Krisanaprakornkit, S. Comparisons between Two Biochemical Markers in Evaluating Periodontal Disease Severity: A Cross-Sectional Study. *BMC Oral Health* **2014**, *14*, No. 107.
(23) Kerschnitzki, M.; Akiva, A.; Ben Shoham, A.; Asscher, Y.; Wagermaier, W.; Fratzl, P.; Addadi, L.; Weiner, S. Bone Mineralization Pathways during the Rapid Growth of Embryonic Chicken Long Bones. *J. Struct. Biol.* **2016**, *195*, 82−92.
(24) Danikowski, K. M.; Cheng, T. Colorimetric Analysis of Alkaline Phosphatase Activity in s. Aureus Biofilm. *J. Vis. Exp.* **2019**, *2019*, No. e59285.
(25) Millán, J. L. Alkaline Phosphatases - Structure, Substrate Specificity and Functional Relatedness to Other Members of a Large Superfamily of Enzymes José. *Purinergic Signal* **2006**, *2*, 335−341.
(26) Kolanczyk, M.; Kossler, N.; Kühnisch, J.; Lavitas, L.; Stricker, S.; Wilkening, U.; Manjubala, I.; Fratzl, P.; Spörle, R.; Herrmann, B. G.; Parada, L. F.; Kornak, U.; Mundlos, S. Multiple Roles for Neurofibromin in Skeletal Development and Growth. *Hum. Mol. Genet.* **2007**, *16*, 874−886.
(27) Chang, C. N.; Kuang, W.-J.; Chen, E. Y. Nucleotide Sequence of the Alkaline Phosphatase Gene of *Escherichia coli*. *Gene* **1986**, *44*, 121−125.
(28) Melamy, M. H.; Horecker, B. L. Amino Acid Sequence of *Escherichia coli* Alkaline Phosphatase. *Biochemistry* **1964**, *3*, 1889−1997.
(29) Okabayashi, K.; Futai, M.; Mizuno, D. Localization of Acid and Alkaline Phosphatases in Staphylococcus Aureus. *Jpn. J. Microbiol.* **1974**, *18*, 287−294.
(30) Luo, H.; Benner, R.; Long, R. A.; Hu, J. Subcellular Localization of Marine Bacterial Alkaline Phosphatases. *Proc. Natl. Acad. Sci. U.S.A.* **2009**, *106*, 21219−21223.
(31) Cosmidis, J.; Benzerara, K.; Guyot, F.; Skouri-panet, F.; Duprat, E.; Férard, C.; Guigner, J.-M.; Babonneau, F.; Coelho, C. Calcium-Phosphate Biomineralization Induced by Alkaline Phosphatase Activity in *Escherichia coli*: Localization, Kinetics, and Potential Signatures in the Fossil Record. *Front. Earth Sci.* **2015**, *3*, No. 84.
(32) Danikowski, K. M.; Cheng, T.; Hong, T.; Kong, A.; Lam, J.; Young, L.; Smirnova, G.; Muzyka, N.; Oktyabrsky, O.; Laboratories, B.; Zhou, Y.; Zhang, T.; Jin, S.; Chen, S.; Zhang, Y.; Hice, S. A.; Santoscoy, M. C.; Soupir, M. L.; Cademartiri, R.; Angkawidjaja, C.; Kuwahara, K.; Omori, K.; Koga, Y.; Takano, K.; Kanaya, S.; Grillo-Puertas, M.; Rintoul, M. R.; Rapisarda, V. A.; Okabayashi, K.; Futai, M.; Mizuno, D. Alkaline Phosphatase Activity of Staphylococcus Aureus Grown in Biofilm and Suspension Cultures. *Curr. Microbiol.* **2018**, *75*, 1226−1230.
(33) Hayashi, K.; Morooka, N.; Yamamoto, Y.; Fujita, K.; Isono, K.; Choi, S.; Ohtsubo, E.; Baba, T.; Wanner, B. L.; Mori, H.; Horiuchi, T. Highly Accurate Genome Sequences of *Escherichia coli* K-12 Strains MG1655 and W3110. *Mol. Syst. Biol.* **2006**, *2*, No. 2006-0007.
(34) Cole, M. F.; Bowen, W. H. The Effect of Calcium β Glycerophosphate on Phosphatase Activity in Plaque from Monkeys (Macaca Fascicularis. *Arch. Oral Biol.* **1974**, *19*, 335−337.
(35) Turesky, S.; Glickman, I.; M, K. Crystal Seeding By Salivary Calculus Inhibition in Vitro. *Arch. Oral Biol.* **1965**, *10*, 255−260.

(36) Sewón, L. A.; Karjalainen, S. M.; Söderling, E.; Lapinleimu, H.; Simell, O. Associations between Salivary Calcium and Oral Health. *J. Clin. Periodontol.* **1998**, *25*, 915−919.
(37) Hoelzl Wallach, D. F.; Surgenor, D. M.; Soderberg, J.; Delano, E. Preparation and Properties of 3, 6-Dihydroxy-2z4-Bis- [KN′-Di-IcarboxymethyO-Aminomethyl] Fluoran. *Anal. Chem.* **1959**, *31*, 456−460.
(38) Fox, E.; Meyer, E.; Panasiak, N.; Taylor, A. R. Calcein Staining as a Tool to Investigate Coccolithophore Calcification. *Front. Mar. Sci.* **2018**, *5*, No. 326.
(39) Vidavsky, N.; Addadi, S.; Mahamid, J.; Shimoni, E.; Ben-Ezra, D.; Shpigel, M.; Weiner, S.; Addadi, L. Initial Stages of Calcium Uptake and Mineral Deposition in Sea Urchin Embryos. *Proc. Natl. Acad. Sci. U.S.A.* **2014**, *111*, 39−44.
(40) Zsiomondy, R. *Kolloidchemie Ein Lehrbuch*; Binz, A., Ed.; Springer-Verlag Berlin Heidelberg GmbH, 1920; Vol. *204*.
(41) van Belle, H. Kinetics and Inhibition of Alkaline Phosphatases from Canine Tissues. *Biochim. Biophys. Acta, Enzymol.* **1972**, *289*, 158−168.
(42) Varghese, Z. Determination of Plasma Calcium Fractions. *Ann. Clin. Biochem.* **1973**, *10*, 120−124.
(43) Vidavsky, N.; Kunitake, J. A. M. R.; Estroff, L. A. Multiple Pathways for Pathological Calcification in the Human Body. *Adv. Healthcare Mater.* **2021**, *10*, No. 2001271.
(44) Keren-Paz, A.; Maan, H.; Karunker, I.; Olender, T.; Kapishnikov, S.; Dersch, S.; Kartvelishvily, E.; Wolf, S. G.; Gal, A.; Graumann, P. L.; Kolodkin-Gal, I. The Roles of Intracellular and Extracellular Calcium in *Bacillus subtilis* Biofilms. *iScience* **2022**, *25*, No. 104308.
(45) Bilecen, K.; Yildiz, F. H. Identification of a Calcium-Controlled Negative Regulatory System Affecting *Vibrio cholerae* Biofilm Formation. *Environ. Microbiol.* **2009**, *11*, 2015−2029.
(46) Sarkisova, S.; Patrauchan, M. A.; Berglund, D.; Nivens, D. E.; Franklin, M. J. Calcium-Induced Virulence Factors Associated with the Extracellular Matrix of Mucoid *Pseudomonas aeruginosa* Biofilms. *J. Bacteriol.* **2005**, *187*, 4327−4337.
(47) Sharma, U.; Pal, D.; Prasad, R. Alkaline Phosphatase: An Overview. *Indian J. Clin. Biochem.* **2014**, *29*, 269−278.
(48) Wanner, B. L. Phosphorus Assimilation and Control of the Phosphate Regulon. In *Escherichia and Salmonella: Cellular and Molecular Biology*; ASM Press: Washington, DC, 1996; pp 1357−1381.
(49) Smith, P.; Schuster, M. Public Goods and Cheating in Microbes. *Curr. Biol.* **2019**, *29*, R442−R447.
(50) Allocati, N.; Masulli, M.; Di Ilio, C.; De Laurenzi, V. Die for the Community: An Overview of Programmed Cell Death in Bacteria. *Cell Death Dis.* **2015**, *6*, No. e1609.
(51) Klauck, G.; Serra, D. O.; Possling, A.; Hengge, R. Spatial Organization of Different Sigma Factor Activities and C-Di-GMP Signalling within the Three-Dimensional Landscape of a Bacterial Biofilm. *Open Biol.* **2018**, *8*, No. 180066.
(52) Eltantawy, M. M.; Belokon, M. A.; Belogub, E. V.; Ledovich, O. I.; Skorb, E. V.; Ulasevich, S. A. Self-Assembled Liesegang Rings of Hydroxyapatite for Cell Culturing. *Adv. NanoBiomed Res.* **2021**, *1*, No. 2000048.
(53) Wang, Y.; Azaïs, T.; Robin, M.; Vallée, A.; Catania, C.; Legriel, P.; Pehau-Arnaudet, G.; Babonneau, F.; Giraud-Guille, M. M.; Nassif, N. The Predominant Role of Collagen in the Nucleation, Growth, Structure and Orientation of Bone Apatite. *Nat. Mater.* **2012**, *11*, 724−733.
(54) Tavafoghi, M.; Cerruti, M. The Role of Amino Acids in Hydroxyapatite Mineralization. *J. R. Soc. Interface* **2016**, *13*, No. 20160462.
(55) Abdali, Z.; Aminzare, M.; Zhu, X.; Debenedictis, E.; Xie, O.; Keten, S.; Dorval Courchesne, N. M. Curli-Mediated Self-Assembly of a Fibrous Protein Scaffold for Hydroxyapatite Mineralization. *ACS Synth. Biol.* **2020**, *9*, 3334−3343.
(56) Azulay, D. N.; Abbasi, R.; Ben Simhon Ktorza, I.; Remennik, S.; Reddy, A. M.; Chai, L. Biopolymers from a Bacterial Extracellular Matrix Affect the Morphology and Structure of Calcium Carbonate Crystals. *Cryst. Growth Des.* **2018**, *18*, 5582−5591.
(57) Thongsomboon, W.; Serra, D. O.; Possling, A.; Hadjineophytou, C.; Hengge, R.; Cegelski, L. Phosphoethanolamine Cellulose: A Naturally Produced Chemically Modified Cellulose. *Science* **2018**, *338*, 334−338.
(58) Saxena, V.; Gao, H.; Arregui, S.; Zollman, A.; Kamocka, M. M.; Xuei, X.; McGuire, P.; Hutchens, M.; Hato, T.; Hains, D. S.; Schwaderer, A. L. Kidney Intercalated Cells Are Phagocytic and Acidify Internalized Uropathogenic *Escherichia coli*. *Nat. Commun.* **2021**, *12*, No. 2405.
(59) Jeffries, J.; Thongsomboon, W.; Visser, J. A.; Enriquez, K.; Yager, D.; Cegelski, L. Variation in the Ratio of Curli and Phosphoethanolamine Cellulose Associated with Biofilm Architecture and Properties. *Biopolymers* **2021**, *112*, No. e23395.
(60) Balasubramanian, S.; Yu, K.; Meyer, A. S.; Karana, E.; Aubin-Tam, M. E. Bioprinting of Regenerative Photosynthetic Living Materials. *Adv. Funct. Mater.* **2021**, *31*, No. 2011162.
(61) Gilbert, C.; Tang, T. C.; Ott, W.; Dorr, B. A.; Shaw, W. M.; Sun, G. L.; Lu, T. K.; Ellis, T. Living Materials with Programmable Functionalities Grown from Engineered Microbial Co-Cultures. *Nat. Mater.* **2021**, *20*, 691−700.
(62) Lagendijk, E. L.; Validov, S.; Lamers, G. E. M.; De Weert, S.; Bloemberg, G. V. Genetic Tools for Tagging Gram-Negative Bacteria with MCherry for Visualization in Vitro and in Natural Habitats, Biofilm and Pathogenicity Studies. *FEMS Microbiol. Lett.* **2010**, *305*, 81−90.
(63) Zizak, I. The MySpot Beamline at BESSY II. *J. Large-Scale Res. Facil. JLSRF* **2016**, *2*, 1−4.
(64) Benecke, G.; Wagermaier, W.; Li, C.; Schwartzkopf, M.; Flucke, G.; Hoerth, R.; Zizak, I.; Burghammer, M.; Metwalli, E.; Müller-Buschbaum, P.; Trebbin, M.; Förster, S.; Paris, O.; Roth, S. V.; Fratzl, P. A Customizable Software for Fast Reduction and Analysis of Large X-Ray Scattering Data Sets: Applications of the New DPDAK Package to Small-Angle X-Ray Scattering and Grazing-Incidence Small-Angle X-Ray Scattering. *J. Appl. Crystallogr.* **2014**, *47*, 1797−1803.

https://doi.org/10.1021/acs.chemmater.2c02969
Chem. Mater. 2023, 35, 2762−2772